Modeling of Multifilament PET Fiber Melt-Spinning

Young-Pyo Jeon, Christopher L. Cox

Center for Advanced Engineering Fibers and Films, Clemson University, Clemson, South Carolina 29634

ABSTRACT: A fundamental issue in the polymer fiber melt-spinning process is the control of final properties. Most available melt-spinning models simulate only a single fiber, providing an incomplete representation of the actual industrial multifilament process. Variations across the fiber bundle in cooling air velocity and temperature result in nonuniformity in fiber properties. Simulation can provide insight into this cause-and-effect relationship and lead to better process design to control differences between fibers. The few multifilament models in existence typically use a Newtonian constitutive model for the polymer, failing to capture nonlinear effects which often play a significant role in the process. Experimental validation of multifilament simulation is lacking. We present a nonisothermal multifilament spinning model, applicable for a variety of polymer and process conditions. The model combines the flow-enhanced crystallization (FEC) fiber spinning model of McHugh et al. with a generalization of Dutta's multifilament model. The model predicts fiber properties such as stress, degree of crystallinity, fiber radius and temperature as a function of distance from the spinneret, along with quench air cross velocity and temperature throughout the fiber bundle region. The McHugh FEC model for single fiber spinning, based on a modified Giesekus constitutive model and Avrami-type crystallization kinetics, has been experimentally validated. In this work we show that results of the multifilament quench air model compare favorably to experimental measurements. © 2008 Wiley Periodicals, Inc. J Appl Polym Sci 110: 2153–2163, 2008

Key words: computer modeling; crystallization; polyesters; multifilament; melt-spinning

INTRODUCTION

One of the most common industrial polymer processes is fiber melt-spinning, in which the polymer melt is extruded through small orifices in the spinneret and drawn into thin fibers by a uniaxial drawing process.

During the more than 40 year growth of the polymer fiber industry, numerous experimental and theoretical efforts have been employed to better understand the melt spinning process. In melt spinning, molecular orientation and crystallization (for semicrystalline polymers) during solidification are closely tied to final fiber properties. Crystallization and orientation depends strongly on fiber temperature, so that the quench process plays a significant role in controlling fiber properties. As pointed out in Ziabicki et al.,[1] experimental data shows that quench properties vary across a multifilament bundle resulting in nonuniform fiber properties. Simulation has the potential to provide valuable insight into the relationship between bundle geometry, melt properties, process conditions, and final fiber properties.

To account for convective heat transfer in their spinning model, Kase and Matsuo[2] proposed an empirical heat transfer coefficient, h_c, which is still widely used. Matsui represented air-drag on the moving fiber by the coefficient C_D, a function of Reynold's number (Re) and spinning velocity[3] (v_z). In addition, Pearson and Richardson[4] simulated the Newtonian behavior of the polymer melt, and Ziabicki et al.[1] modeled the process using a Maxwell fluid model. While most efforts in the published literature focus on single filament spinning, some[5,6,7] investigated multifilament spinning. These three papers each simulate PET fiber spinning using a Newtonian constitutive model. On-line experimental measurements for multifilament spinning are found in Ziabicki[8] and Andreassen et al.,[9] though details are insufficient for validation of simulation results.

Several models have been developed to describe crystallization during the spinning process, including the models of Katayama et al.,[10] Patel et al.,[11] and Ziemenski and Spruiell[12] which combine crystallization kinetics with the Newtonian constitutive equation for the polymer melt. For high-speed melt spinning, the so-called flow-induced (stress-induced) crystallization (FIC) occurs as a result of high tensile stresses in the fibers. The FIC fiber spinning model of McHugh and coworkers[13–15] incorporates crystallization with strain-softening and strain-hardening associated with nonlinear viscoelastic effects which

produce a necking phenomenon. An updated version of this model which avoids a numerical singularity sometimes found in the earlier approach is presented by Shrikhande et al.[16]

Most models to date lack sufficient detail to adequately describe the industrial melt-spinning process, because they simulate only a single filament or they are based on a Newtonian constitutive equation. Harvey and Doufas[17] recently introduced a multifilament fiber-spinning model by coupling a single fiber model with a three-dimensional Navier-Stokes computational fluid dynamics (CFD) solution for the quench regime. Although being the most detailed model to date for multifilament fiber spinning, no comparisons were made with experimental results and the simulation requires extensive CPU time and memory. The paper of Zhang et al.[7] is based on an approach similar to the current effort. The model described herein differs in the incorporation of a viscoelastic constitutive model and semicrystalline effects.

The purpose of this article is to present a multifilament fiber melt-spinning model which includes viscoelastic effects and semicrystalline behavior in a nonisothermal multifilament setting. A secondary goal is to develop a model which will run on a desktop computer in reasonable time. The calculated quench properties, as affected by the fiber bundle, are validated against experimentally measured values. The rest of this article is organized as follows. In "Multifilament model development" Section the governing equations for the fibers and quench air are developed. Simulation results, including comparison with experimental data, are provided in "Results and discussion" Section. Conclusions and an outline of continuing work are presented in "Conclusions" Section.

MULTIFILAMENT MODEL DEVELOPMENT

Our approach is a generalization of that in Dutta's.[6] The Newtonian constitutive model[6] used for each fiber is replaced with the flow-enhanced crystallization (FEC) model of McHugh et al.,[16] thereby allowing for effects associated with viscoelastic flows and crystallization. Whereas, Dutta assumed that the air density is constant, we explore the effect of a temperature-dependent density on simulation results. In this section the governing equations for the FEC fiber spinning model are presented, followed by our version of the multifilament approach. The McHugh FEC fiber spinning model was chosen for the current study because it provides results which correlate favorably with on-line experimental data while requiring relatively small computing resources. The equations governing the crystalline phase depend on model parameters which must be calibrated against

one set of experimental data. This feature is not restrictive for the current effort, since a change in quench properties does not require an update of the model parameters. One limitation of the fiber spinning model is the assumption that all properties vary only in the axial direction. Radial variations in temperature and crystallinity are not accounted for. It is also worth noting that the fundamental theory of polymer crystallization is still being developed. Therefore, the microstructural model employed in this study is not a first principles model. Yet it is a major advancement over earlier models in the way in which structure (molecular orientation and crystallinity) is coupled with temperature, velocity, and stress. Simulations results match experimental on-line data over the spectrum of process conditions, including at high speeds where the necking phenomenon occurs. A full development of the FEC model can be found in the papers of McHugh et al.[13–16]

Single filament model: FEC model

The 1D FEC model uses the radially-averaged conservation equations, as developed in Pearson and Richardson,[4] so the dependent variables are functions only of axial distance z from the spinneret. We assume that the flow is steady-state and that the polymer density, ρ, is constant. Letting z, v_z, A, and W denote distance from the spinneret, axial velocity, fiber cross-sectional area, and mass flow rate, respectively, the steady-state form of the mass conservation equation is then

$$W(z) = \rho v_z A(z) = W_0 \tag{1}$$

where, the subscript '0' denotes values at the spinneret face (e.g. $W_0 = W(0)$ and $v_0 = v_z(0)$). Let the superscript '*' denote dimensionless quantities, so that $v_z^* = v_z/v_0$, $\tau^* = \tau/G_0$, (dimensionless extra stress tensor), and $z^* = z/L$. Then the dimensionless momentum conservation equation is written as

$$D_1 v_0^* \frac{dv_z^*}{dz^*} = -\frac{D_4}{\sqrt{v_z^*}}\frac{dv_z^*}{dz^*} + \frac{d\left(\tau_{zz}^* - \tau_{rr}^*\right)}{dz^*}$$
$$- D_2 v_z^*(v_z^* - v_d^*) + D_3 \tag{2}$$

where, in particular $\tau_{zz}^* - \tau_{rr}^*$ is the dimensionless tensile stress. The dimensionless quantities D_1, D_2, D_3, and D_4 are defined in Table I. The material and process parameters comprising D_1, D_2, D_3, and D_4 (including G_0) are defined in Tables II and III.

The stress term in eq. (2) is calculated as a function of x, the relative degree of semicrystalline transformation, and components of the microstructural

TABLE I
Dimensionless Constants Used in Governing Equations, as Defined in [13], Unless Otherwise Noted

Definition	Description
$D_1 = \dfrac{\rho v_0^2}{G_0}$	Inertia
$D_2 = \dfrac{\pi \mu^{air} BL\rho v_0^2}{GA_0}$	Air drag
$D_3 = \dfrac{gL\rho}{G_0}$	Gravity
$D_4 = \left(\dfrac{\pi s^2}{4A_0 G_0^2}\right)^{1/2}$	Surface tension
$D_5 = \left(\dfrac{2\pi L^2 h_c^2}{\rho^2 A_0 C_p^2 v_0^2}\right)^{1/2}$	Convective heat transfer
$D_6 = \dfrac{G_0}{\rho C_p T_0}$	Viscous dissipation
$D_7 = \dfrac{\Delta H_f \varphi_\infty}{C_p T_0}$	Latent heat of crystallization
$De_{sc} = \dfrac{cv_0 \eta_0(T) \exp(Fx)}{LG}$	Semi-crystalline phase Deborah number
$De_a = (1-x)^2 \dfrac{v_0 \lambda_a}{L}$	Scaled melt phase Deborah number
$B = 0.185 \left(\dfrac{\rho^{air} v_z D}{\mu^{air}}\right)^{0.39}$	Bingham number, [8]

tensors c and S, i.e.

$$\tau_{zz}^* - \tau_{rr}^* = \frac{c_{zz}^* - c_{rr}^*}{1-x} + 4.5 S_{zz} + 6De_{sc}(B_{zz} - B_{rr}) \quad (3)$$

where,

$$B_{zz} = \left[(1-\omega)\left(\frac{2}{15} + \frac{11}{14}S_{zz}\right) + \omega\frac{3}{2}S_{zz}\left(s_{zz} + \frac{1}{3}\right)\right]\frac{dv_z^*}{dz^*} \quad (4)$$

$$B_{rr} = \left[(1-\omega)\left(-\frac{1}{15} + \frac{4}{14}S_{zz}\right) \right.$$
$$\left. + \omega\frac{3}{2}S_{zz}\left(-\frac{s_{zz}}{2} + \frac{1}{3}\right)\right]\frac{dv_z^*}{dz^*} \quad (5)$$

and

$$\omega = 1 - 27\det\left(S + \frac{1}{3}\delta\right) \quad (6)$$

In eqs. (3)–(5), S is the semicrystalline orientation tensor and $c^* = cK/(k_BT)$ is the dimensionless melt phase conformation tensor, in which K is the elastic dumbbell spring constant and k_B the Boltzmann constant. The form of De_{sc} in eq. (3), defined in Table I, is developed in Doufas and McHugh.[13] In De_{sc}, the orientational relaxation time of the semicrystalline phase is defined as $\lambda_{sc} = c\lambda_a \exp(Fx)$ where, c and F are model parameters which are determined from experimental data, and λ_a, appearing in the Deborah number of the melt De_a, is calculated by dividing the zero-shear-rate viscosity by the shear modulus.

The zero-shear-rate viscosity of the melt used in our version of the model takes the form of the Arrhenius equation,

$$\eta_0(T) = \eta_A \exp\left(\frac{\eta_B}{T}\right) \quad (7)$$

This expression is similar to those used in Shrikhande et al.[16] In dimensionless form, conservation of energy is expressed as

TABLE II
Material Parameters used for Simulations

Symbol (units)	Name	Value
ρ (g/cm^3)	Polymer density	1.36
G_0 (Pa)	Melt shear modulus	9.52e4
α (-)	Mobility parameter	0.3
s (dyne/cm)	Surface tension	35
η_A (Pa·s)	Used in zero-shear-rate viscosity	3.3e−4
η_B (K)	Used in zero-shear-rate viscosity	7,570
ϕ_∞ (-)	Ultimate degree of crystallinity	0.42
K_{max} (s^{-1})	Maximum crystallization rate	0.016
T_{max} (C)	Maximum crystallization rate temperature	190
D_{av} (C)	Crystallization rate curve half-width	64
C_{s1} [cal/(g·°C)]	Coefficient in crystalline part of C_p	0.2502
C_{s2} [cal/ (g· (°C)^2)]	Coefficient in crystalline part of C_p	0.0007
C_{s3} [cal/(g· (°C)^3)]	Coefficient in crystalline part of C_p	0
C_{l1} [cal/(g·°C)]	Coefficient in amorphous part of C_p	0.3243
C_{l2} [cal/(g· (°C)^2)]	Coefficient in amorphous part of C_p	5.65e−4
C_{l3} [cal/(g·(°C)^3)]	Coefficient in amorphous part of C_p	0
$\Delta H_f(0)$ (cal/g)	Reference heat of fusion	30

TABLE III
Process Parameters Used for Simulations

Symbol (units)	Name	Sim. I	Sim. II	Sim. III
T_0 (°C)	Spinneret temperature	285	285	310
W (kg/min/hole)	Mass flow rate	7e−4	5.231e−4	2.8e−3
D_0 (mm)	Capillary diameter	0.4	0.231	0.4
v_z (m/min)	Take-up speed	1,200	1,371	5,500
L (m)	Spinline length	0.8	0.813	2
T^{air} (°C)	Upwind air temperature	25	35	25
v_{c0}^{air} (m/sec)	Upwind air cross velocity	0.6	Function of z	2.0
v_{d0} (m/min)	Upwind air downward velocity	0	0	0
z_1 (m)	Quench zone start	0	0.02	0
z_2 (m)	Quench zone end	0.8	0.43	2.0
M	Number of rows	10	10	10
h_1 (mm)	Distance between rows	3.5	2.935	15
h_2 (mm)	Distance between holes	7.2	1.589	10

$$\frac{dT^*}{dz^*} = -\frac{D_5}{\sqrt{v_z^*}}(T^* - T_a^*) + D_6\left(\frac{\tau_{zz} - \tau_{rr}}{v_z}\right)\frac{dv_z^*}{dz^*} + D_7\frac{dx}{dz} \quad (8)$$

where, T^* is the nondimensionalized polymer temperature, $T^* = T/T_0$ and T_a^* is the nondimensionalized air temperature at the fiber surface. The right hand side of eq. (8) is formulated to account for the influence of heat transfer from the fiber surface, energy of deformation associated with stress and deformation rate, and heat of phase transformation.[4] Dimensionless parameters D_5, D_6, and D_7 are defined in Table I. The heat capacity and heat of fusion are expressed as polynomial functions of temperature, in the form

$$C_p(T) = (C_{s1} + C_{s2}T + C_{s3}T^2)x\phi_\infty$$
$$+ (C_{l1} + C_{l2}T + C_{l3}T^2)(1 - x\phi_\infty) \quad (9)$$

and

$$\Delta H_f(T) = \Delta H_f(0) + (C_{l1} - C_{s1})T + (C_{l2} - C_{s2})\frac{T^2}{2}$$
$$+ (C_{l3} - C_{s3})\frac{T^3}{2} \quad (10)$$

Heat transfer is assumed to be dominated by the convective part. The empirical correlation for the heat transfer coefficient, h_c, proposed by Kase and Matsuo[2] is used in the form

$$h_c = 0.42k\left(\frac{v_z}{D^2\mu^{air}}\right)^{1/3}\left[1 + \left(\frac{8v_c^{air}}{v_z}\right)^2\right]^{1/6} \quad (11)$$

where, k is heat conductivity, μ^{air} is air viscosity, v_c^{air} is cross-flow quench air velocity, v_z is axial fiber spinning velocity, and D is fiber diameter.

Additionally, the model requires four equations related to microstructural variables: three equations for components of the conformation and orientation tensors and an equation for the relative degree of crystallinity $x = \phi/\phi_\infty$, where ϕ and ϕ_∞ are the absolute and ultimate degree of crystallinity, relatively. These equations are

$$\frac{dc_{zz}^*}{dz^*} = 2\frac{c_{zz}^*}{v_z^*}\frac{dv_z^*}{dz^*} - \frac{1-x}{v_z De_a}\left((1-\alpha) + \alpha\frac{c_{zz}^*}{1-x}\right)\left(\frac{c_{zz}^*}{1-x} - 1\right) \quad (12)$$

$$\frac{dc_{rr}^*}{dz^*} = -\frac{c_{rr}^*}{v_z^*}\frac{dv_z^*}{dz^*} - \frac{1-x}{v_z De_a}\left((1-\alpha) + \alpha\frac{c_{rr}^*}{1-x}\right)\left(\frac{c_{rr}^*}{1-x} - 1\right) \quad (13)$$

$$\frac{dS_{zz}}{dz^*} = \left(\frac{2}{3} + 2S_{zz}\right)\frac{1}{v_z^*}\frac{dv_z^*}{dz^*} - \frac{1}{v_z^* De_{sc}}S_{zz} - 2\frac{B_{zz}}{v_z^*} \quad (14)$$

and

$$\frac{dx}{dz^*} = \frac{K^*}{v_z^*}(1-x)\exp(2\xi a^*) \quad (15)$$

where, ξ is the flow coupling parameter and a^* is the dimensionless stored free energy, $a^* = a/G_0$, of the amorphous phase, satisfying the equation

$$\frac{da^*}{dz^*} = \frac{c^* : \nabla^* v_z^*}{v_z^*(1-x)} - \frac{a^*}{v_z^* De_a} \quad (16)$$

The temperature dependence of the Avrami factor for crystallization, $K^* = K_{av}L/v_0$, is approximated as a Gaussian function, i.e.

$$K_{av}(T) = K_{max}\exp\left[-4\ln(2)\frac{(T - T_{max})^2}{D_{av}^2}\right] \quad (17)$$

Multifilament approach

Fibers in a multifilament setting may experience a wide variation in quench conditions depending on location in the fiber bundle. Heat transfer between the fibers and quench air will result in warmer quench air towards the leeward side of the fiber bundle. In addition, since the air is a compressible fluid, heating of the quench air will result in volume expansion and density reduction. In the

multifilament environment, the amount of air being dragged downwards by the moving fibers is not negligible, so that downward air flow should be accounted for along with cross air flow. The variation of quench conditions between fibers will likely produce a variation in fiber properties.

Dutta[6] introduced a simple multifilament melt spinning model describing nonuniform quench conditions. To describe the effect of nonidentical quench conditions on fiber properties, Dutta established simple mass and energy balance equations based on Matsui's expression of the downward air velocity.[3] The downward air velocity (v_d) being dragged by a moving fiber with velocity, v_z, obtained by Matsui is

$$v_d = v_z \left\{ 1 - \int\limits_{\Psi}^{1} \frac{C_D \cdot Re_D}{\psi + [\psi^2 + \lambda(1 - \psi^2)^2]^{1/2}} d\psi \right\} \quad (18)$$

where Ψ is a dimensionless radius ($\Psi = \sqrt{r_f/r}$), Re_D is the Reynold's number ($Re_D = D\rho v/\mu$), C_D is the drag coefficient ($C_D = 1.22K^{0.78}Re_D^{-0.61}$ and $K = 0.22$), and λ is a constant being related to Prandtl's mixing length ($\lambda = K^2 Re_D^2 C_D/2$). Based on the air drag estimated by Matsui,[3] Dutta[6] calculated the downward air mass flow rate (q) by integrating the downward air velocity v_d:

$$q = 2\pi\rho^{air} \int\limits_{r_f}^{r_{eff}} rv_d dr \quad (19)$$

where, r_f is fiber radius. The effective radius for each fiber zone, r_{eff}, can be determined based on the fiber distribution in the spinneret. If fibers are uniformly distributed in the spinneret, the effective radius is determined by the area of the spinneret divided by the number of fibers:

$$r_{eff} = \sqrt{\frac{Spinneret\_area}{\pi N}}$$

Combining eqs. (18) and (19) gives a complete expression for the downward air mass flow rate,

$$q = 4\pi\rho^{air}r_f^2 v_z$$

$$\int\limits_{r_f}^{\psi_{eff}} \psi^{*3}\left\{ 1 - \int\limits_{\psi^*}^{1} \frac{C_D \cdot Re_D}{\psi + [\psi^2 + \lambda(1 - \psi^2)^2]^{1/2}} d\psi \right\} d\psi^* \quad (20)$$

The dimensionless effective radius, ψ_{eff}, is defined as $\psi_{eff} = \sqrt{r_{eff}/r_f}$.

Similar to Dutta,[6] we define a computational cell as shown in Figure 1 to describe the quench air temperature and cross velocity distributions. In Fig-
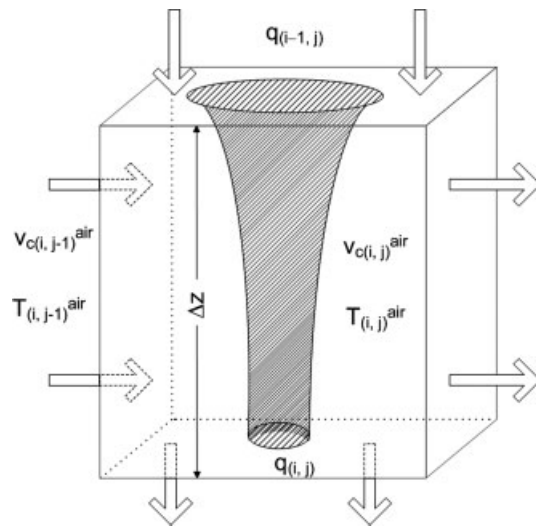

Figure 1 A schematic diagram of a computational cell containing a filament section.

ure 1, the subscripts i and j denote the segment number (in the spinline direction) and the row number, respectively. A mass balance is imposed on each cell, i.e.

$$(\rho^{air}v_c^{air}A_c)_{(i,j-1)} + q_{(i-1,j)} = (\rho^{air}v_c^{air}A_c)_{(i,j)} + q_{(i,j)} \quad (21)$$

where, A_c is the area of the cell border perpendicular to the primary direction of the quench air flow and the (i,j) subscript refers to the cell from which respective quantities originate. Solving for $v_{c,(i,j)}^{air}$ in eq. (21) results in

$$v_{c(i,j)}^{air} = \frac{v_{c(i,j-1)}^{air}\rho_{(i,j-1)}^{air}A_{c(i,j-1)}}{\rho_{(i,j)}^{air}A_{c(i,j)}} - \frac{q_{(i,j)} - q_{(i-1,j)}}{\rho_{(i,j)}^{air}A_{c(i,j)}} \quad (22)$$

As in Dutta,[6] it is assumed that there is no lateral variation in quench properties, i.e., all fibers in a row experience the same air velocity and temperature. In contrast to Dutta,[6] air density is allowed to vary with temperature, according to the formula

$$\rho^{air} = \frac{P_d}{R_d T} \quad (23)$$

which follows from the Ideal Gas Law for dry air, where P_d is 1 atm (101,325 Pa), R_d is the specific gas constant for dry air [287.05 J/(Kg K)], and T is in Kelvin units.

The spinneret and quench system used in Dutta[6] are displayed in Figure 2. Top and lateral views are displayed to illustrate the relationship of the quench flow to the spinline.

We now write an energy balance equation on the computational cell in Figure 1. the energy input and output are
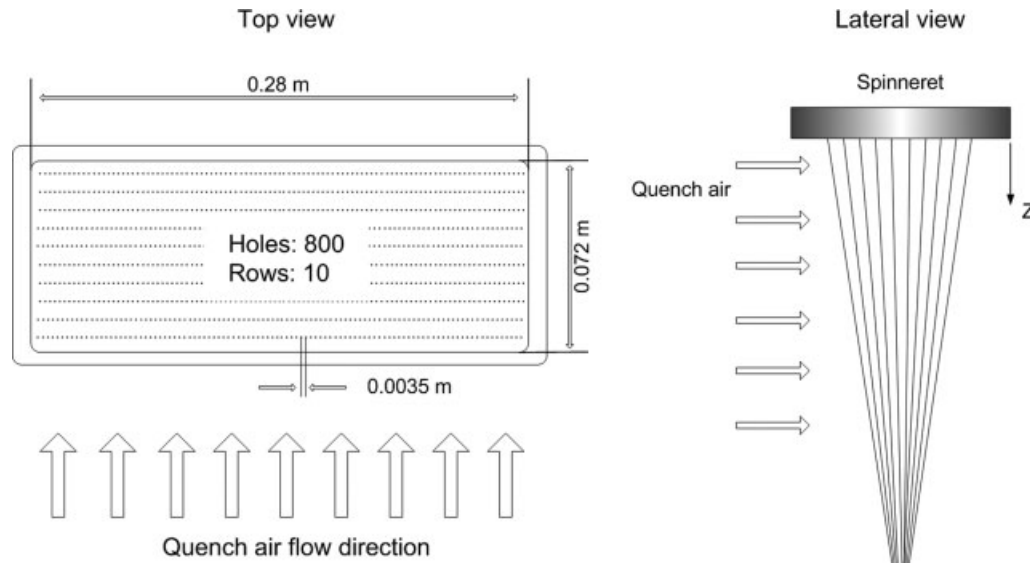
Figure 2 Quench air flow to the system (top view and lateral view).

$$E_{in} = WC_pT_{(i-1,j)} + \rho^{air}_{(i,j-1)}v^{air}_{c(i,j-1)}A_{c(i,j-1)}C^{air}_{p(i,j-1)}T^{air}_{(i,j-1)}$$

$$+ 0.5q_{(i-1,j)}(C^{air}_{p(i-1,j-1)}T^{air}_{(i-1,j-1)} + C^{air}_{p(i-1,j)}T^{air}_{(i-1,j)}) \quad (24)$$

$$E_{out} = WC_pT_{(i,j)} + \rho^{air}_{(i,j)}v^{air}_{c(i,j)}A_{c(i,j)}C^{air}_{p(i,j)}T^{air}_{(i,j)}$$

$$+ 0.5q_{(i,j)}(C^{air}_{p(i,j-1)}T^{air}_{(i,j-1)} + C^{air}_{p(i,j)}T^{air}_{(i,j)}) \quad (25)$$

where, the heat capacity for air is calculated as in Smith et al.[18]

$$C^{air}_p = 1.9327 \times 10^{-10}T^4 - 7.9999 \times 10^{-7}T^3$$

$$+ 1.1047 \times 10^{-3}T^2 - 4.4890 \times 10^{-1}T + 1.0575 \times 10^3 \quad (26)$$

As developed in Dutta,[6] the three terms on the right hand sides of eqs. (24) and (25) represent heat due to the polymer, heat due the quench air flowing transversely, and heat due to the air pumped downwards, respectively. Again we allow density to vary with temperature. Equating the right hand sides of eqs. (24) and (25) and solving for $T^{air}_{(i,j)}$ results in

$$T^{air}_{(i,j)} = \frac{WC_p[T_{(i-1,j)} - T_{(i,j)}] + \rho^{air}_{(i,j-1)}v^{air}_{c(i,j-1)}A_{c(i,j-1)}C^{air}_{p(i,j-1)}T^{air}_{(i,j-1)}}{C^{air}_{p(i,j)}[\rho^{air}_{(i,j)}v^{air}_{c(i,j)}A_{c(i,j)} + 0.5q_{(i,j)}]}$$

$$+ \frac{0.5q_{(i-1,j)}[C^{air}_{p(i-1,j-1)}T^{air}_{(i-1,j-1)} + C^{air}_{p(i-1,j)}T^{air}_{(i-1,j)}] - 0.5q_{(i,j)}C^{air}_{p(i,j-1)}T^{air}_{(i,j-1)}}{C^{air}_{p(i,j)}[\rho^{air}_{(i,j)}v^{air}_{c(i,j)}A_{c(i,j)} + 0.5q_{(i,j)}]} \quad (27)$$

RESULTS AND DISCUSSION

We now present simulation results for three cases: the spinneret and process conditions from Dutta,[6] then a circular spinneret and process conditions provided by an industry source, and a high-speed variation on the first case. The polymer used in each case is PET (Polyethylene Terephthalate), with material parameters listed in Table II.

Equations (2), (8), and (12)–(16) are solved for the dependent variables pertaining directly to the fibers.

In light of eq. (3), eq. (2) is a second order differential equation in v^*_z, so that an additional equation is introduced to complete a first order system in the variables v^*_z, dv^*_z/dz^*, T^*, c^*_{zz}, c^*_{rr}, S_{zz}, x, and a^*. Initial values of dv^*_z/dz^*, c^{**}_{rr}, and S_{zz} are determined using the procedure outlined in Shrikande, et al.[16] Equations (22) and (27) are used to solve for the air cross-velocity and temperature, respectively. These two systems of equations (one for the fibers, one for the quench air) are solved in iterative fashion, beginning
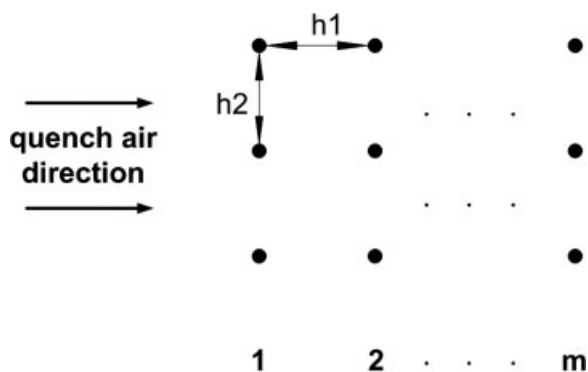
Figure 3 Spinneret hole arrangement for simulation.

with solution of the fiber equations with quench conditions not varying between the fibers. Integrals in eq. (20) are evaluated using Simpson's rule with 10 intervals. Convergence is reached in two or three iterations. The Matlab code takes less than 30 min to execute on a desktop PC.

Simulation I: Comparison to Dutta's results

For this case we consider the spinneret and process conditions in Dutta.[6] The spinneret is shown in Figure 2 and the process conditions are listed in the first column of numbers in Table III. The parameters governing the spinneret hole spacing are defined in Figure 3.

Figure 4 contains comparisons between Dutta's calculations and the current model predictions of quench air velocity and temperature. Results of the current model agree qualitatively with Dutta's calculations, but not quantitatively, especially in row 10. Differences in these results are due both to the incorporation of temperature-dependent air density and a viscoelastic constitutive equation in the current model (in contrast to the viscous model used by Dutta).
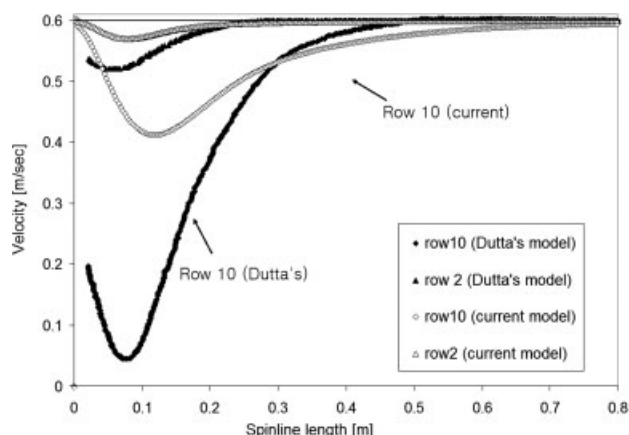
Predictions of fiber temperature and stress for both models are compared in Figure 5. There is a near match of temperature profiles for row 1, with differences increasing in subsequent rows. Stress profiles show higher values in the current model, especially on the cooler side. This could be due to viscoelastic effects, which play a role in necking behavior,[1] and is possibly also related to a slight amount of crystallinity ($\phi \approx 10^{-3}$) present in the first row of fibers. Figure 6 illustrates variations in fiber velocity between rows. The variations in quench air properties have a strong influence on fiber properties.

Simulation II: An industrial circular spinneret

We now compare our results to experimental data measured on-line in an industrial setting. The single filament model of McHugh et al. has been experimentally validated.[13–16] Therefore, a key requirement of a multifilament model, which incorporates the McHugh model for each fiber, is to accurately predict quench properties.

On-line quench air velocity and temperature measurements were collected at a Wellman, fiber spinning plant.[19] The spinneret geometry and quench zones relative to the spinline are illustrated in Figure 7. The PET melt is extruded through a spinneret with holes arranged in 10 rings, each containing 300 capillaries. We approximate the hole arrangement with a rectangular spacing by averaging in the radial direction. Process conditions, including hole spacings used in the model, are listed in the second column of numbers in Table III. As shown in Figure 7, the quench profile consists of an active quench zone (0.41 m in length) where air is distributed by the quench diffuser to the fibers, followed by the air entrainment zone (0.43 m long) where the velocity of the quench air was measured
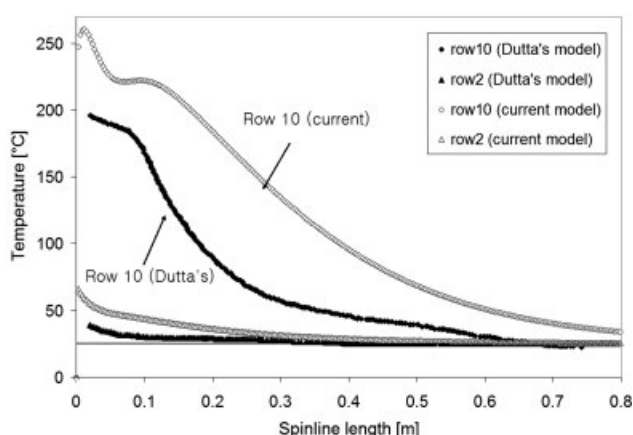

Figure 4 Comparisons of quench air velocity and temperature with Dutta's calculation (take-up velocity is 1,200 m/min).
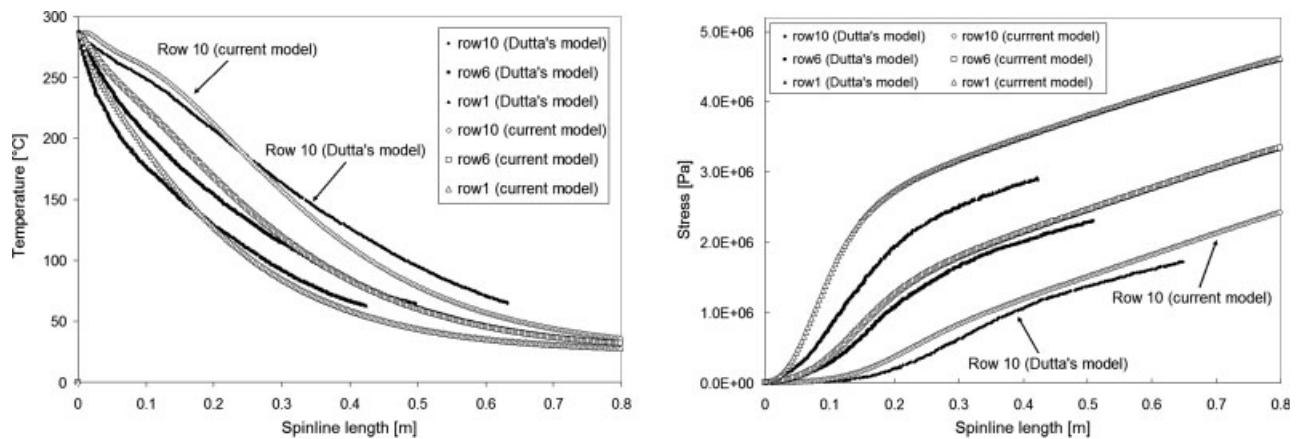
Figure 5 Comparisons of fiber temperature and stress with Dutta's calculation (1,200 m/min take-up velocity).
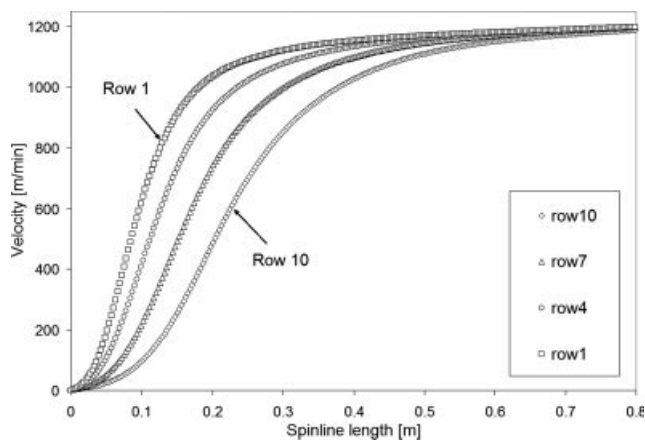

Figure 6 Calculated fiber axial velocity, at 1,200 m/min take-up velocity.

as 0.1 m/s. Quench air speed transverse to and upwind of the fiber bundle was measured at several points along the spinline. These values are plotted in Figure 8. A piecewise linear fit of this data, using three lines, was used as the inflow condition for quench air in the model. Also shown in Figure 8 are the calculated air cross-velocities in rows 4, 7, and 10. The other set of experimental measurements provided to us consists of quench air temperature on the downwind side of the bundle, at 5 points along the spinline. Calculated temperature profiles for rows 1, 4, 7, and 10 are plotted along with the experimental measurements in Figure 8. The calculated temperatures for row 10 compare favorably with the experimental data. Calculated fiber properties are similar to those in the previous case (Figs. 5 and 6).
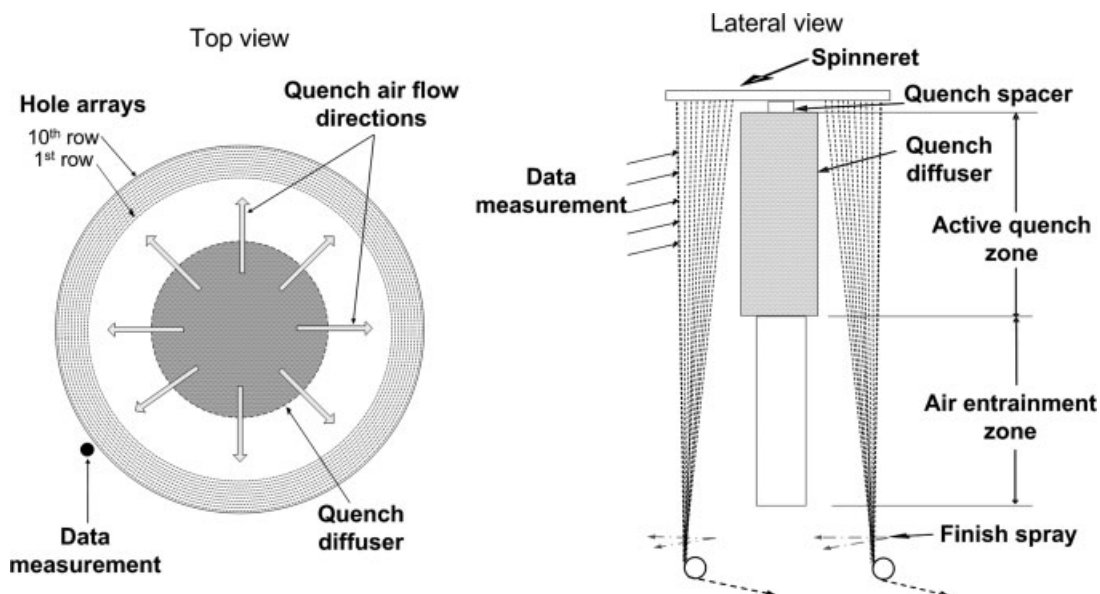

Figure 7 Geometry of the Wellman spinneret (top view and lateral view).
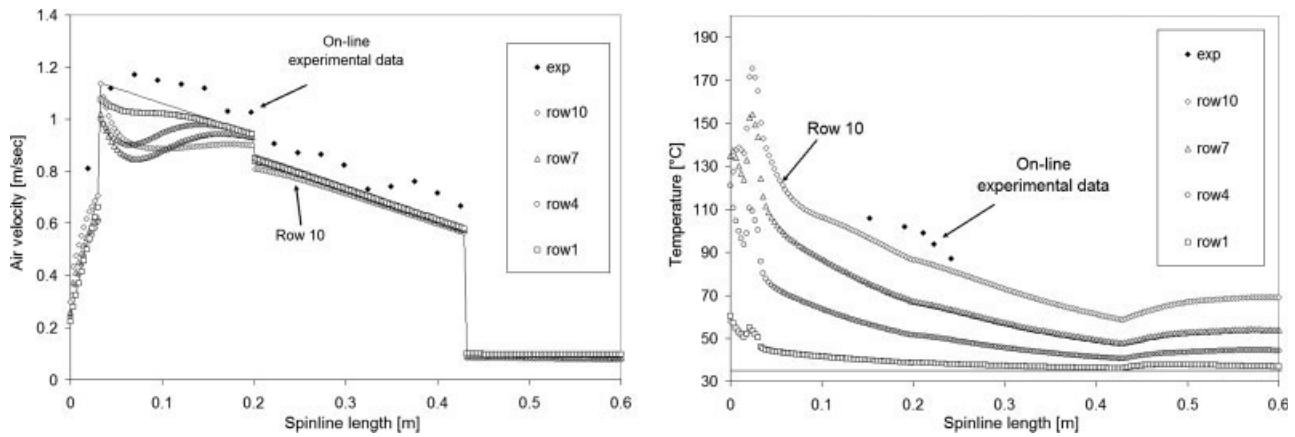
Figure 8 Simulation results of quench velocity and temperature for the Wellman Spinneret at 1,371 m/min take-up velocity.

In both cases, as expected, percent crystallinity was negligible (around 10^{-4} or less).

Simulation III: High speed spinning

We now simulate high-speed spinning to examine the scenario in which the semicrystalline fraction is non-negligible. Process conditions for this case are listed in Table III. Simulation results for fiber speed, temperature, crystallinity, and stress are plotted in Figure 9. Properties of the quench air (temperature, cross and downward velocity components, and downward flow rate) are presented graphically in Figure 10. The variation in quench air conditions between rows resulted in significant variation in fiber characteristics. The start of the 'plateau' region
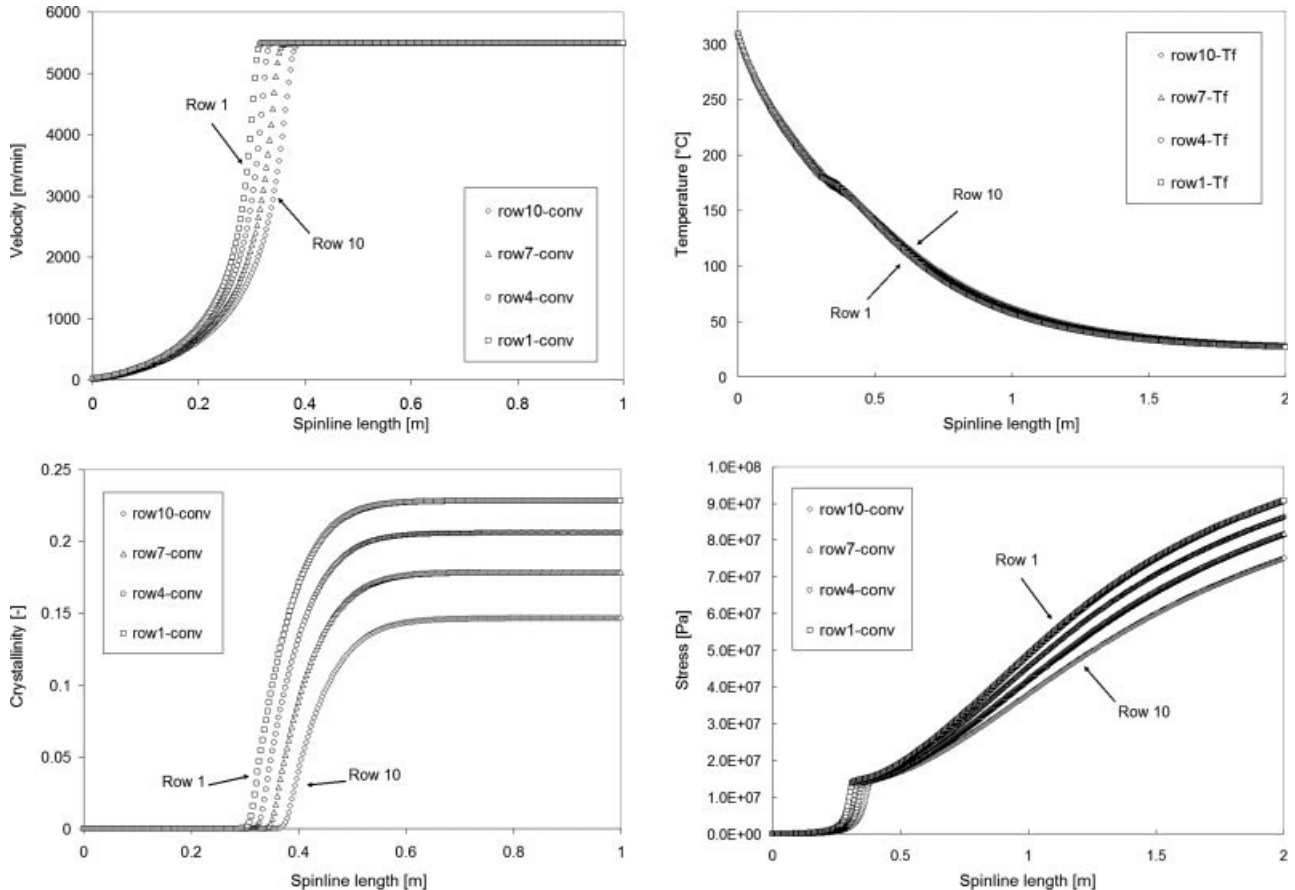

Figure 9 Simulation results of fiber characteristics for high-speed spinning: fiber speed, temperature, crystallinity, and tensile stress.
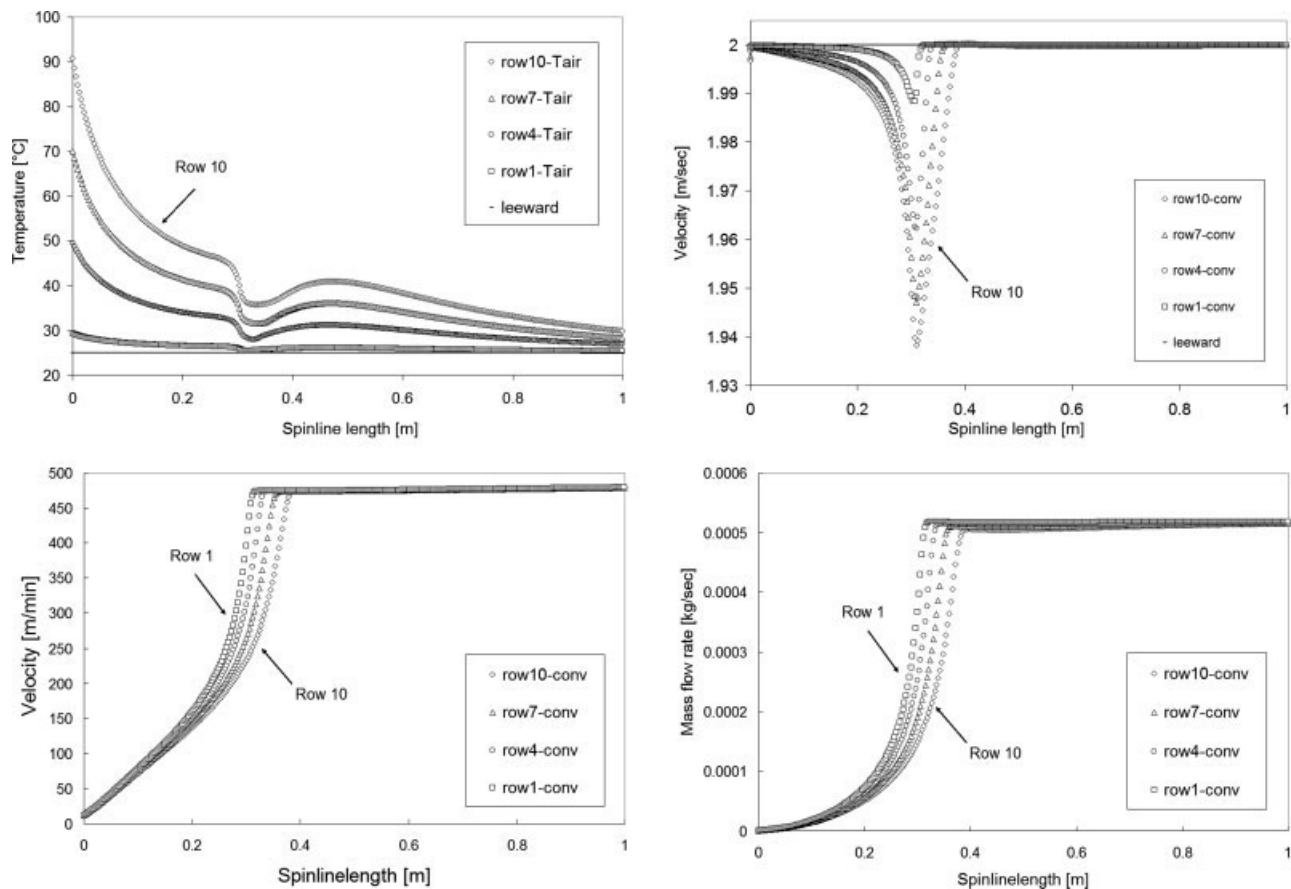
Figure 10 Simulation results of quench air properties for high-speed spinning: quench air temperature, cross velocity, downward velocity, and downward mass flow rate.

in the fiber velocity varies from row to row. The final degree of crystallinity in row 1 fibers is 50% higher than in row 10 fibers. This result correlates with warmer temperature and lower stress values in row 10 than in row 1.

CONCLUSIONS

We have presented a multifilament melt spinning model that incorporates effects of viscoelasticity and crystallization in the fiber model, and convective heat transfer in the quench environment. The model runs in 30 min or less on a desktop computer. Comparisons with the previously published model of Dutta indicate that the models provide qualitatively similar results but differ quantitatively especially with respect to computed quench air properties and fiber stress through the bundle. Comparisons of model results with industry measurements for air temperature on the downwind side of the bundle indicated a difference of ~ 10%, which is especially significant considering the wide variation of air temperature through the bundle. Few such comparisons

exist in the current literature. Model results at high speeds with significant crystallization are also provided. The variation of quench properties through the fiber bundle for this case correspond to variations in fiber attributes, including a difference in the degree of crystallinity in the fibers which would be associated with nonuniformities in final fiber properties.

The simulation code will be generalized to accommodate other spinneret geometries such as a staggered arrangement of holes. Additional experimental validation is warranted, at various process conditions and for a variety of polymers. The sensitivity of results to FEC model parameters c, F, and ξ will be explored. The effect of radiative heat transfer, especially relative to convective heat transfer, will also be considered.

References

1. Ziabicki, A.; Jarecki, L.; Wasiak, A. Comput Theor Polym Sci 1998, 8, 143.
2. Kase, S.; Matsuo, T. J Appl Polym Sci 1967, 11, 251.
3. Matsui, M. Trans Soc Rheol 1976, 20, 465.
4. Pearson, J. R. A.; Richardson, S. M. Computational Analysis of Polymer Processing; Applied Science Publishers: London and New York, 1983.
5. Tung, L.; Ballman, R.; Nunning, W.; Everage, A. Computer simulation of commercial melt spinning process, The Third Pacific Chemical Engineering Congress 1982, pp 21.
6. Dutta, A. Text Res J 1987, 57, 13.
7. Zhang, C.; Wang, C.; Wang, H.; Zhang, Y. J Macromol Sci Phys 2007, 46, 793.
8. Ziabicki, A. Fundamental Studies of Fiber Formation; Academic Press 1979, Vol. 3, pp 235.
9. Andreassen, E.; Myhre, O. J.; Oldervoll, R.; Hinrichsen, E. L.; Grostad, K.; Braathen, M. D. J Appl Polym Sci 1995, 58, 1619.
10. Katayama, K.-I.; Yoon, M.-G. High-speed Fiber Spinning; Wiley: New York, 1985.
11. Patel, R. M.; Bheda, J. H.; Spruiell, J. E. J Appl Polym Sci 1991, 42, 1671.
12. Ziemenski, K. F.; Spruiell, J. E. J Appl Polym Sci 1988, 35, 2223.
13. Doufas, A. K.; McHugh, A. J.; Miller, C. J Non-New Fluid Mech 2000, 92, 27.
14. Doufas, A. K.; McHugh, A. J.; Miller, C.; Immaneni, A. J Non-New Fluid Mech 2000, 92, 81.
15. Doufas, A. K.; McHugh, A. J. J Rheol 2001, 45, 403.
16. Shrikhande, P.; Kohler, W. H.; McHugh, A. J. J Appl Polym Sci 2006, 100, 3240.
17. Harvey, A. D.; Doufas, A. K. AIChE J 2006, 53, 78.
18. Smith, J. M.; Van Ness, H. C.; Abbott, M. M. Introduction to Chemical Engineering Thermodynamics, 6th ed.; McGraw-Hill, 2001.
19. Private Communication, Wellman, Charlotte, NC, USA, 2007.